SAND2021-7684C

Second mode growth in a high-velocity boundary layer using stability theory and DNS

Shaun R. Harris[*] and Ross M. Wagnild[†]
Sandia National Laboratories, Albuquerque, NM 87185

Direct numerical simulations (DNS) were conducted of a high-velocity flat plate boundary layer with time-periodic fluctuating inflow. The DNS fluctuation growth and evolution over the plate is then compared to the solution as computed using classical linear stability theory (LST) and the parabolized stability equations (PSE) of a second mode eigenfunction. The agreement observed between the eigenfunction from LST and the fundamental harmonic of the temporal Fourier transform (FT) of the DNS simulation demonstrates the ability of the solver to capture the initiation and linear growth of a hypersonic boundary layer instability. The work enables the study of the perturbation's evolution in the boundary layer as well as provides confidence in the numerical solver to study further development towards non-linear growth and eventual transition to turbulence.

I. Nomenclature

BL = boundary layer
C = generic coefficient
δ_{99} = 99% boundary layer thickness
FT = Fourier transform
LST = Linear Stability Theory
M = million
q = state vector of velocities and pressure
$\hat{q}$ = Fourier transform coefficient of state vector
PSE = Parabolized Stability Equations
RMS = Root mean square
sdist = streamwise distance along the flat plate
SPARC = Sandia Parallel Aerodynamics and Reentry Code
STABL = Stability and Transition Analysis for hypersonic Boundary Layers
t = time (s)
u, v, w = streamwise, wall-normal, and spanwise velocities (m/s)
x, y, z = streamwise, wall-normal, and spanwise dimensions (m)

II. Introduction

In hypersonic flight, the laminar to turbulent transition has a large impact in the heat transfer across an atmospheric flight vehicle. Understanding this process has the potential to lead to significant advancement in the design, cost, and capability of the vehicle. As outlined in a recent review article [1] the transition process changes as freestream disturbances are increased. In the low disturbance environment of flight, eigenmode growth is believed to be the dominant process underlying boundary layer transition. This path to transition shows how eigenmode growth is the dominant mechanism leading to nonlinear breakdown and eventually transition to turbulence. In high-velocity flight conditions, stability theory indicates that Mack's second mode instabilities are often the dominant modes leading to the initial modal interactions. Modeling this growth can be done using a combination of linear stability theory (LST) and the parabolized stability equations (PSE). Using those stability methods allows for predictions of the second mode growth and decay in laminar flow for relatively inexpensive computational cost. These methods restrict one to pure laminar flow

---

[*] R & D Graduate Intern, Computational Thermal and Fluid Mechanics, Student Member.

[†] Principal Member of the Technical Staff, Aerosciences Department, Senior Member AIAA.

Sandia National Laboratories is a multimission laboratory managed and operated by National Technology & Engineering Solutions of Sandia, LLC, a wholly owned subsidiary of Honeywell International Inc., for the U.S. Department of Energy's National Nuclear Security Administration under contract DE-NA0003525.

and small amplitude perturbations that do not excite modal interactions or the transition process. In order to calculate the full transition process from laminar to turbulent, one requires a more expensive approach such as using direct numerical simulation (DNS). This DNS approach allows for accurately capturing low-amplitude disturbances modeled in a boundary layer and compares well with PSE analysis. Additionally, the DNS approach can capture nonlinear interactions for high-amplitude disturbances and the full transition process to turbulence. Modeling the full transition process will be valuable in understanding the various sensitivities of the transition process in these flow regimes. To gain confidence in the simulation and methods, we turn our attention in this work to the linear and low-amplitude perturbation growth.

This work utilizes the Sandia Parallel Aerodynamics and Reentry Code (SPARC) [2] on a hypersonic flow condition with perturbation growth in a boundary layer as the DNS solver. SPARC is the next-generation transonic and hypersonic CFD code that supports high performance computing and performance portability for a variety of computer architectures including GPU platforms. The software solves either the perfect or the reacting Navier-Stokes equations and has several discretization methods capable of standard hypersonic numerics as well as low dissipation methods for DNS. For these computations, we are using the perfect gas solver using Sutherland's law for viscosity and a constant Prandtl number for thermal conductivity. The Subbareddy-Candler [3] inviscid-flux scheme was utilized. The tunnel experiment uses nitrogen, therefore, the gas simulated in these simulation uses the properties of nitrogen.

For the linear stability analysis, a suite of tools for stability calculations and analysis of hypersonic boundary layers known as Stability and Transition Analysis for hypersonic Boundary Layers (STABL) [4] will be utilized. The geometry used in these calculations is an ideal flat plate. Using STABL, a frequency matching the largest second mode growth is chosen for the specified flow conditions. The inflow to the DNS simulation is then set at this frequency with a uniform in space and time-periodic perturbation. The resulting flow over the flat plate is then compared to the anticipated growth of the second mode calculated using the LST and PSE from STABL.

The flow conditions of interest were chosen to match the experiment performed in Sandia's HWT wind tunnel for a hypersonic sharp cone [5]. However, this initial work focuses on comparing the perturbation growth in a flat plate boundary layer. Comparisons between experimental and simulation conditions can be performed by making use of Mangler transform [6] that states the boundary layer is a factor of $\sqrt{3}$ thinner for a cone than for a flat plate. The transition and growth could be directly compared for a cone and boundary layer using this transform, but is not studied in this work at this time. The state conditions for this flat plate hypersonic boundary-layer are shown in Table 1.

Table 1 Freestream conditions chosen for this study to compare to experiment in Table 1. of [5]. We include the freestream Mach number, the Reynolds number, the stagnation pressure, and the stagnation temperature.

M_∞ (-)	Re (10^6 1/m)	P_0 (kPa)	T_0 (kelvin)
7.9	13.4	4692.2	617.8

III. Methods

We outline the conditions and methods for both LST and DNS used to estimate the growth of the second mode eigenvalue in a boundary layer at the specified flow conditions.

A. LST and PSE

LST and PSE are popular choices for estimating the eigenmode growth in a boundary layer due to the accuracy and relatively inexpensive computation. For LST, we assume a locally parallel base flow and the ansatz,

$$\mathbf{q} = \hat{\mathbf{q}}(y)e^{i(\alpha x+\beta z-\omega t)} + c.c., \tag{1}$$

is substituted into the linearized Navier-Stokes equations where $c.c.$ indiactes the complex conjugate. Neglecting non-parallel and non-linear terms leads to an eigenvalue problem of the form

$$\mathcal{L}\hat{\mathbf{q}} = \alpha\hat{\mathbf{q}}. \tag{2}$$

We solve this eigenvalue problem at a range of frequencies and locations along the plate to get an idea of the expected growth and decay of various modes. Plotting the growth rate (imaginary part of the streamwise wavenumber α and

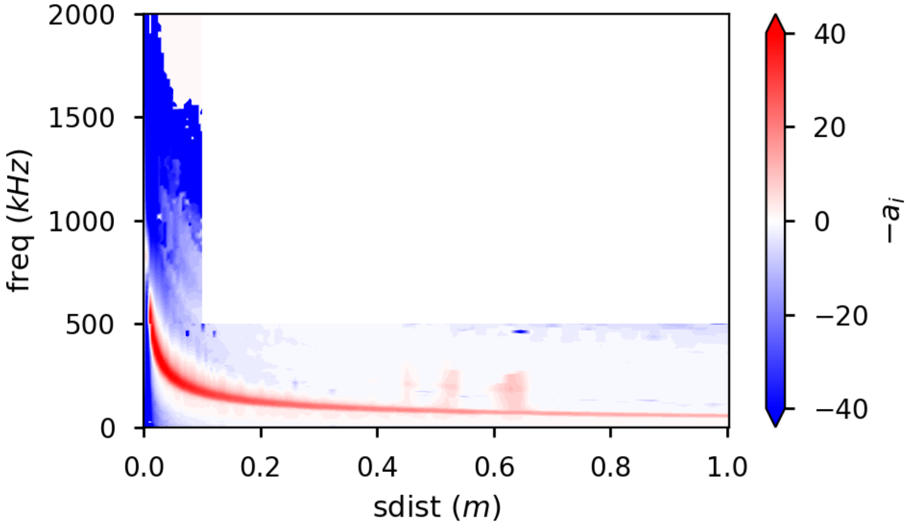

Fig. 1 STABL stability diagram for the given flight conditions ($\mathbf{a}_i = \alpha_i$)

eigenvalue) gives the following stability diagram shown in Fig. 1. The strong growth shown around the 100's kHz range for a majority of the length studied is caused by the second mode instability. Fluctuations in this frequency range tend to see large amplification and in several high-speed flows, this is the dominant eigenmode observed. PSE relaxes the parallel flow assumption of LST by utilizing a non-parallel baseflow and uses the ansatz

$$\mathbf{q} = \hat{\mathbf{q}}(x, y)e^{i(\int \alpha dx + \beta z - \omega t)} + c.c. \tag{3}$$

Neglecting small and non-linear terms from the linearized Navier-Stokes Equations we arrive at the PSE that can be marched downstream using an integration technique [7]. It should be noted that the solution procedure is unstable due to remaining ellipticity in the governing equations and a remedy must be used to eliminate the remaining ellipticity. A summary of these possible remedies can be found in the work by [8]. Of the possible remedies suggested there, STABL uses the pressure gradient suppression to stabilize the marching procedure. The PSE are used to march the eigenfunctions identified in the LST analysis downstream and the mode with the largest overall growth is identified. The resulting LST values near the leading edge of the plate is presented in Table 2.

Table 2 STABL parameters of the second mode instability

x (m)	α (rad/m)	β (1/m)	$f = \frac{\omega}{2\pi}$ kHz
0.05	591.2+3.4i	0	91.2

The N factor is an estimate of the growth of the perturbation magnitude and can be used as an indicator for transition scenarios. This N factor is estimated using PSE from the kinetic energy of the perturbation integrated along the wall-normal direction along with the growth rate integrated across the streamwise direction as shown Eq. 4 below.

$$\sigma = -\alpha_i + \frac{1}{E}\frac{dE}{dx} \tag{4a}$$

$$E = \int \overline{\rho}(|\hat{u}|^2 + |\hat{v}|^2 + |\hat{w}|^2)dy \tag{4b}$$

$$N = \int_{x_0}^{x} \sigma dx \tag{4c}$$

The anticipated N factor growth as estimated by PSE is shown in Fig. 13 alongside the DNS results that are discussed below.

B. DNS

One major focus of this work is to validate the SPARC solver's ability to calculate the linear growth of the second mode instability present at these flow conditions. Therefore, SPARC was used to mimic the PSE process by calculating the same flow conditions with a fluctuating inlet of different types. A series of case studies each with three separate simulations are presented in this work with varying boundary conditions and complexity.

The first is a two-dimensional simulation over the entire plate including some of the freestream region ahead of the plate. The boundary condition ahead of the leading edge is a symmetry plane entrance region before the physical wall takes on a no-slip condition. A low-amplitude uniform perturbation was initialized at the inflow as to not excite nonlinear interactions as it progresses downstream.

The acoustic forcing inlet in SPARC is used for the first calculation. The boundary condition is formulated using an eigenvalue approach to solving the linearized, compressible Euler equations and follows the derivation in [9]. Eigenvalues for each of the disturbance types, slow acoustic, fast acoustic, entropy, and vorticity can be computed by starting from the linearized 2D Euler equations and inputting a peturbation of similar form as above:

$$\mathbf{q} = \hat{\mathbf{q}} e^{i(\alpha x + \beta z - \omega t)}, \tag{5}$$

where ε is the wall-normal wavenumber of the wave. The angle of incidence of the wave to the x-direction, θ, is used to compute the wall-normal wave number using the relation

$$\varepsilon = \alpha * \tan(\theta)\,. \tag{6}$$

Using these formulas, the dispersion relation for a slow acoustic wave becomes

$$\alpha = \frac{\omega}{\bar{u} + \bar{v} * \tan(\theta) - c * \sqrt{1 + \tan^2(\theta)}}, \tag{7}$$

where $\bar{u}$ and $\bar{v}$ are the base state axial and wall-normal velocity components, respectively, and c is the speed of sound. The eigenvector for the slow acoustic wave is

$$\lambda = \left\{ \begin{array}{c} -\frac{\bar{\rho}}{c}\alpha\sqrt{1 + \tan^2(\theta)} \\ \alpha \\ \varepsilon \\ -\bar{\rho} c \alpha \sqrt{1 + \tan^2(\theta)} \end{array} \right\}. \tag{8}$$

In order to make each disturbance type of similar magnitude, each eigenvector is normalized by a relevant base state gas quantity such as

$$\|\lambda\| = \sqrt{\left(\frac{\lambda_\rho}{\bar{\rho}}\right)^2 + \left(\frac{\lambda_u}{\|\bar{\mathbf{u}}\|}\right)^2 + \left(\frac{\lambda_v}{\|\bar{\mathbf{u}}\|}\right)^2 + \left(\frac{\lambda_p}{\bar{\rho}\,\|\bar{\mathbf{u}}\|^2}\right)^2}, \tag{9}$$

where $\bar{\mathbf{u}}$ is the base state velocity vector. Lastly, the freestream magnitudes are computed using the normalized eigenvalues with a fractional value, η, to set the amplitude as in

$$\left\{ \begin{array}{c} \hat{\rho} \\ \hat{u} \\ \hat{v} \\ \hat{p} \end{array} \right\} = \eta \left\{ \begin{array}{c} \lambda_\rho \\ \lambda_u \\ \lambda_v \\ \lambda_p \end{array} \right\} / \|\lambda\|\,. \tag{10}$$

The result is that entropy waves are normalized by the base state density and temperature, vorticity waves are normalized by the base state velocity and disturbance wave number magnitude, and the acoustic waves are normalized by the Mach number and the disturbance wave number magnitude. Traditionally, acoustic forcing amplitudes have been normalized by the freestream pressure, however, with this method the specification is the fraction of the full eigenvalue amplitude. For the slow acoustic forcing, the relationship between the eigenvalue amplitude and the pressure amplitude is

$$\eta = \frac{\hat{p}}{\bar{p}} * \frac{\sqrt{M^4 + M^2 + 1}}{\gamma M^2} \tag{11}$$

This simulation, referenced by the term acoustic, contains a single uniform acoustic perturbation given ahead of the flat plate. The mesh contained 10.1 M control volumes and was two-dimensional by making the spanwise periodic dimension only two cells wide. This type of two-dimensional spanwise treatment is used for all cases that are labelled 2D.

The second simulation type consisted of a smaller domain where the inflow was altered to match the second mode eigenfunction and matching frequency identified from STABL with the respective boundary layer. This reduced the computational expense by decreasing the number of control volumes to roughly 5.4 M for the two-dimensional grid. This simulation grid was used in two case studies or six separate simulations with varying inlet profiles and streamwise locations. One case study investigated one point just beyond the start of the leading edge of the plate with varying magnitude of the perturbation. This location lies just before the neutral point in the LST modal growth and corresponds to the values in Table 2. This case study provided confidence for SPARC to capture the linear growth using these inflow conditions as well as observe some initial nonlinear growth. The other case study investigated three other points further downstream for this same second mode. These three simulations helped to build confidence in the boundary condition used in this study and the ability to be utilized further downstream during the growth phase of the modal growth.

The third domain started downstream of the neutral point, and contained significant spanwise resolution. The increased resolution was used to validate the three-dimensional capability to capture the linear growth of the two-dimensional eigenmode and matching growth. This was used in preparation to test a larger amplitude case where nonlinear breakdown and eventual transition would be possible. This grid contained roughly 679 M control volumes.

All domains consisted of a rectangular volume discretized using rectangular finite volumes. To ensure accuracy of the calculation, the grid was clustered to the wall with a $\Delta y^+ = 1$ chosen in the boundary layer for the duration of the plate. The grid is also clustered to the start of the plate and then the streamwise spacing is relaxed to include roughly 50 points per period of the specified second mode, resulting in a $\Delta x^+ = 26$ streamwise spacing. For the three-dimensional simulation the spanwise resolution matched the streamwise resolution. The outlet of the domain contained rapid growth in the streamwise cell sizes to act as a buffer layer and reduce upstream traveling accoustic waves in the simulation. Thus, any items plotted beyond a streamwise location of $x = 0.54$ should be considered as non-physical due to the extreme stretching. A fourth order Runge-Kutta time integration was used to advance the flow approximately 6 flow-through times allowing the perturbations advecting from the inlet to reach a consisent maximum amplitude along the full lenght of the plate. The time-step used for the simulation allowed for 2000 points per period of the fundamental frequency.

The growth for the respective fluctuations are also compared to the growth anticipated from LST. The N-factor for the fluctuation quantities from SPARC can be computed by the wall pressure perturbation RMS value by

$$N = \int_{x_0}^{x} \frac{1}{P_{rms}} \frac{dP_{rms}}{dx}\, dx + C. \tag{12}$$

Here, the C coefficient is used to shift the growth lines for comparison against the growth computed using LST from STABL as shown in Eq. 4. Since this is a linear growth, this type of shift can be used for the comparison purposes.

IV. Results

The final state of the boundary layer and streamwise perturbations are shown in Fig. 2 for a specific time instant for the 2D acoustic simulation. The other simulations have very similar qualitative appearance and are not shown for brevity. In this figure we observe the growth of the boundary layer alongside the initiation and growth of the second mode instability. The colored circles in Fig. 2 show the local maximum disturbance amplitude (in the wall-normal dimension) at a few specified streamwise locations. We take the FT at each of these locations and plot the magnitude of the coefficients as a function of the frequency. These colored circles match the colors of the FT coefficients shown in Fig. 3 for those same locations.

We can see the magnitude of the second harmonic in Fig. 3 is orders of magnitude smaller than the fundamental harmonic, thus it shows that these cases are mostly linear. Since the nonlinear coefficients are small, comparison to linear growth is acceptable here as the second harmonics don't alter the linear growth in a significant manner. It should also be noted that the other simulations had lower-amplitude fluctuations and thus were even more linear than this case as will be shown below. The following results will show similar plots and FT analysis for three case studies.

A. Case study: amplitude

In this case study, we have a 2D inlet that is just prior to the neutral point of the eigenmode as calculated from STABL. The amplitude of the eigenvalue at the inflow condition, amp, varies from 0.1, to 0.001. This amplitude is

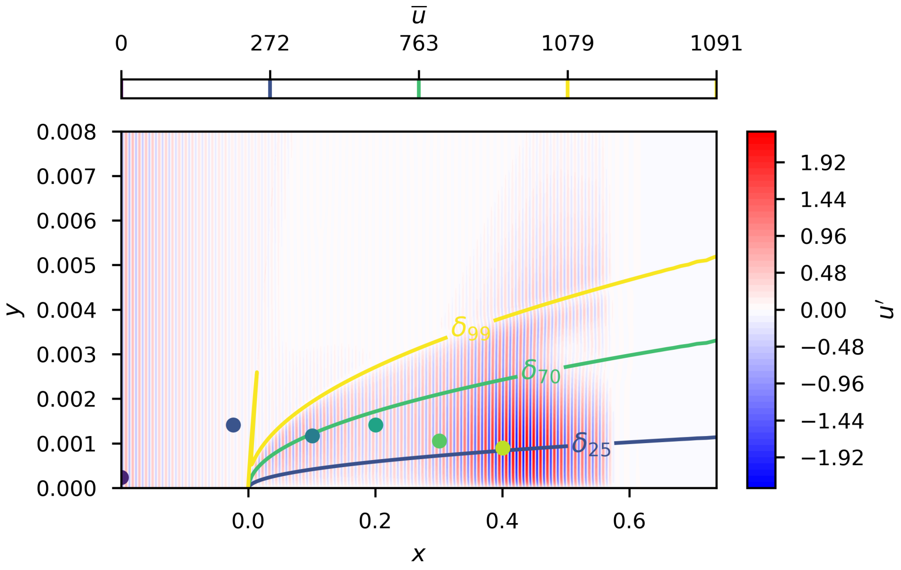

Fig. 2 DNS results using SPARC with a uniform periodic inflow. Contour lines show average streamwise velocity at several boundary layer locations, colored domain shows streamwise perturbations at a single time instant. The colored dots indicate the maximum local streamwise RMS value wall-normal location at various streamwise locations. The colors of these dots match with the FT magnitude shown in Fig. 3.

multiplied by the normalized eigenfunction and fed into SPARC on three separate simulations along with the respective boundary layer. Once steady state was achieved after 6 flow through times, the resulting streamwise RMS values can be seen in Fig. 4. We can see from this figure, that the relative magnitude of the perturbations matches the order of magnitude of the amplitude given at the inflow condition. All three of these cases are nearly linear as can be observed by analyzing the matching FT plots shown in Fig. 5 The largest amplitude case studied here only shows minor nonlinear growth, and the smallest amplitude cases demonstrates a purely linear case.

The growth of these modes can be seen by looking at the N-factor and comparing it to the anticipated values from LST. The DNS N-factor has been shifted in the y-axis for aid in comparing multiple DNS results to a single LST. This same shifting is done in all following N-factor plots. Since DNS contains nonlinear calculations, this kind of shifting is not proper, but is used here for comparison purposes only. This N-factor comparison is shown in Fig. 6

As seen in Figs. 4, 5, and 6, after an initial transient, the growth of the eigenmode is nearly identical to what is anticipated from LST. This is a common attribute to all cases where we used a STABL calculated eigenmode as the inlet to SPARC.

B. Case study: streamwise location

Another set of three 2D simulations were conducted where the second mode was calculated at three separate streamwise locations. The resulting streamwise RMS perturbations are shown in Fig. 7. Again, after the initial transient behavior, the perturbation matches the expected modal growth anticipated from LST. The matching FT are shown in 8 with the respective N-factor shown in Fig. 9

We again observe the transient behavior followed by good agreement between LST and SPARC results. This study provided confidence in the BL inlet condition to provide an adequate method to initialize a SPARC simulation with a second mode past the neutral point and still observe growth that matches the anticipated LST.

C. Case study: acoustic, 2D, and 3D

A comparison of the RMS of the streamwise fluctuation for the acoustic inflow simulation, the 2D eigenfunction inlet simulation, and the 3D eigenfunction inlet simulation can be seen in Fig. 10. We have chosen to show the lowest amplitude 2D inlet case from the first case study. This figure also presents a good visual of the three separate inflow locations. The vertical colored lines identify the various streamwise locations where the second mode from STABL is

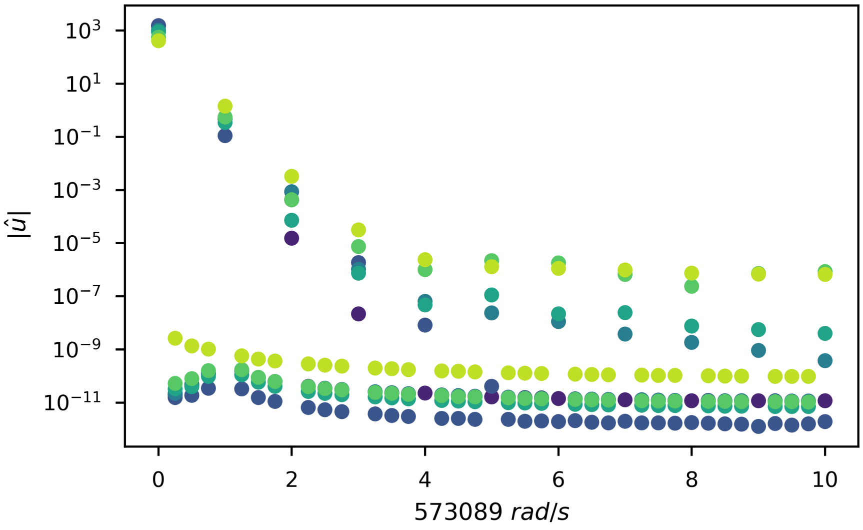

Fig. 3 FT coefficients in time as a function of temporal frequency of the DNS results using SPARC. The colored dots match with the dots and locations shown in Fig. 2 for the simulation domain.

compared to the FT fundamental harmonic of the matching frequency.

Fig. 12 shows how the shape of the FT fundamental mode in the SPARC simulations compares well to the shape of Mack's second mode from STABL at various streamwise locations. We note here, that the magnitude of the individual modes needed to be scaled for proper qualitative comparison. It is also observed that the magnitude of fundamental harmonic in the 2D acoustic simulation at $x = 0.046$ away from the boundary layer is much higher than what is predicted by LST while still resembling the second mode in the boundary layer. This is due to the fact that our inlet to this simulation is uniform in the wall-normal direction and retains some magnitude at locations far from the boundary layer. However, as one moves further downstream, we observe that this acoustic mode dissipates away far from the boundary layer and matches the LST prediction. Additionally, the 3D BL inlet profile at $x = 0.26$ seems to retain some transient behavior as it doesn't match the LST prediction that well, however, as one moves further downstream we see that it collapses back to the expected shape. This shows that after an initial transient behavior, that the BL inlet allows for excellent comparison between LST and DNS simulations using SPARC.

Comparing the respective growth for the simulations and LST, in Fig. 13, shows good agreement except for the acoustic inflow simulation, which experiences less growth. This is most-likely due to the different dissipation switch used in the simulation. The acoustic inflow case utilized the Mach dissipation switch [10]. The BL inlet simulations used the Ducros [11] dissipation switch. It is known that the minimum dissipation level of the Mach switch is noticeably higher than that of the Ducros switch in the boundary layer. It is most likely that this increase in dissipation led to the lower growth rate observed in the acoustic simulation, but not in the other simulations. The initial transient at the two eigenfunction inflow simulations can be observed, but the main growth of the second mode is easily comparable across all simulations with exception of the acoustic inflow simulation.

All of the cases studied here have compared well to linear studies. The amplitude of the RMS of the wall pressure of the 3D inlet simulation can be seen in Fig. 14. The peak amplitude is 100 times smaller than the anticipated value of 28% that would lead to transition to turbulence as observed by [12] for similar flight conditions. Thus, future analysis will use this linear result with an increased amplitude to study the nonlinear breakdown and transition to turbulence in the full 3D environment.

V. Conclusion

In this work, eight DNS simulations with varying complexity and boundary conditions compare well for both the growth and shape of perturbations in a high speed boundary layer when compared to LST. The current work demonstrates the ability of the SPARC flow solver to accurately capture the initiation and linear evolution of Mack's second mode in

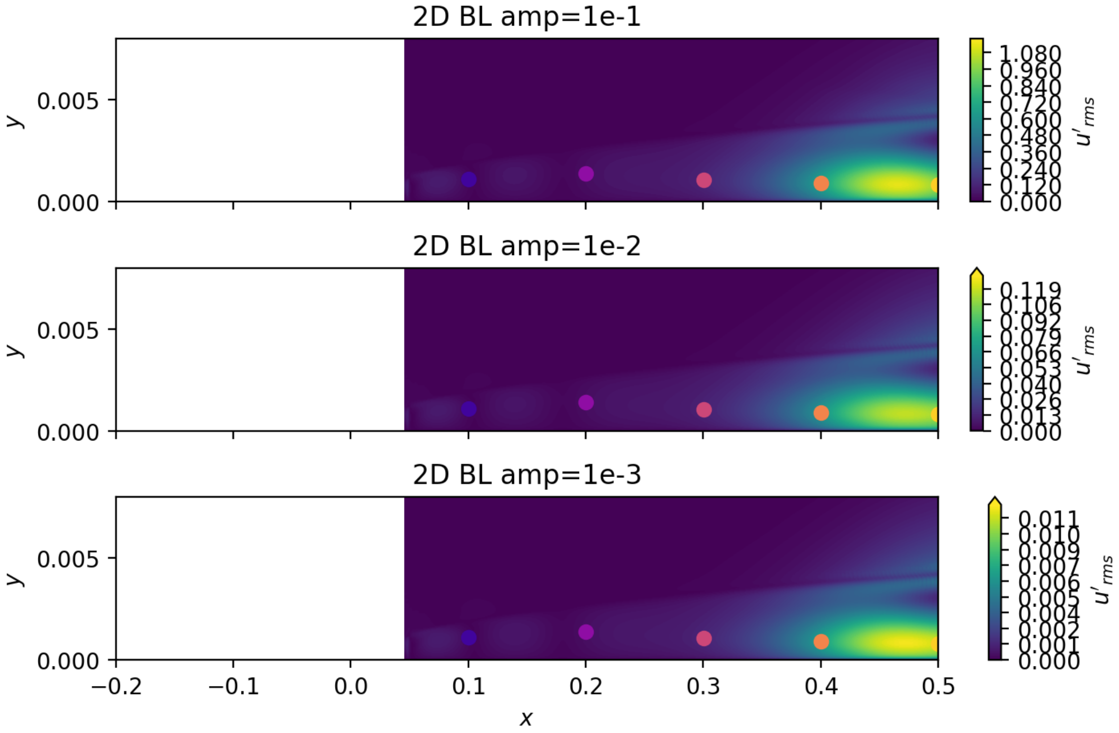

Fig. 4 Streamwise velocity perturbation RMS values for the first case study varying the amplitude on the 2D inlet case. The relative amplitudes ranged a couple orders of magnitude as indicated by the subtitles of each contour. The colored dots indicate the locations of the FT coefficients shown in Fig. 5

2D and 3D simulations, which is the dominant perturbation for the conditions chosen. The fundamental harmonic from a FT of the DNS simulations compares well to the anticipated eigenmode at various streamwise locations after an initial transient from the inflow boundary. The linear growth and matching N factors also build confidence in the method of generating and studying the second mode growth using SPARC. With this gained confidence in the numerical method and conditions, further studies involving nonlinear growth and eventual transition will be investigated in the full 3D environment. Together, these studies will provide further physical insight into perturbation growth and the transition process at these hypersonic flow conditions.

Acknowledgments

The authors would like to thank Neal Bitter from Johns Hopkins Applied Physics Laboratory for the insights, feedback, and guidance regarding the LST and DNS. Sandia National Laboratories is a multi-mission laboratory managed and operated by National Technology and Engineering Solutions of Sandia, LLC., a wholly owned subsidiary of Honeywell International, Inc., for the U.S. Department of Energy's National Nuclear Security Administration under contract DE-NA0003525.

References

[1] Fedorov, A., "Transition and Stability of High-Speed Boundary Layers," *Annual Review of Fluid Mechanics*, Vol. 43, No. 1, 2011, pp. 79–95. https://doi.org/10.1146/annurev-fluid-122109-160750, URL https://doi.org/10.1146/annurev-fluid-122109-160750.

[2] Howard, M., Bradley, A., Bova, S. W., Overflet, J., Wagnild, R., Dinzl, D., Hoemmen, M., and Klinvex, A., "Towards Performance Portability in a Compressible CFD Code," American Institute of Aeronautics and Astronautics (AIAA), 2017.

[3] Subbareddy, P. K., and Candler, G. V., "A fully discrete, kinetic energy consistent finite-volume scheme for compressible flows," *Journal of Computational Physics*, Vol. 228, No. 5, 2009, pp. 1347–1364. https://doi.org/10.1016/j.jcp.2008.10.026, URL https://doi.org/10.1016/j.jcp.2008.10.026.

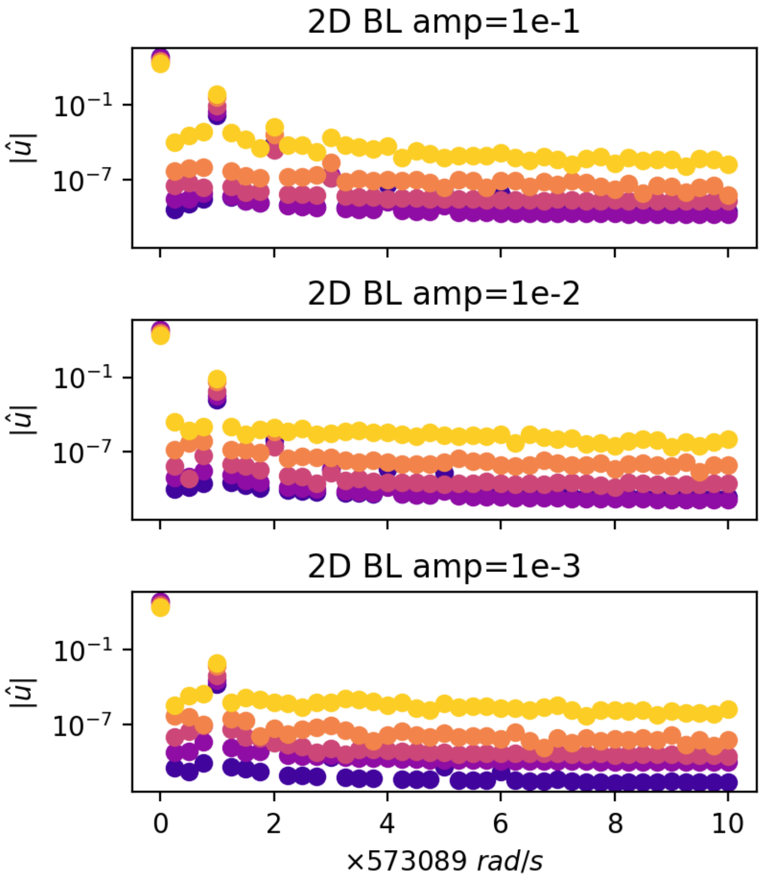

Fig. 5 Streamwise FT coefficient magnitude at the matching colored dots from Fig. 4.

[4] Johnson, H., and Candler, G., "Hypersonic Boundary Layer Stability Analysis Using PSE-Chem," 35th AIAA Fluid Dynamics Conference and Exhibit, 2005. https://doi.org/10.2514/6.2005-5023.

[5] Smith, J. A., DeChant, L. J., Casper, K. M., Mesh, M., and Field, R. V., "Comparison of a Turbulent Boundary Layer Pressure Fluctuation Model to Hypersonic Cone Measurements," American Institute of Aeronautics and Astronautics (AIAA), 2016. https://doi.org/10.2514/6.2016-4047.

[6] Malik, M. R., and Spall, R. E., "On the stability of compressible flow past axisymmetric bodies," *Journal of Fluid Mechanics*, Vol. 228, 1991, p. 443–463. https://doi.org/10.1017/S002211209100277X.

[7] Herbert, T., "Parabolized stability equations," *Annu. Rev. Fluid Mech.*, Vol. 29, 1997, pp. 245–283.

[8] Towne, A., Rigas, G., and Colonius, T., "A critical assessment of the parabolized stability equations," *Theoretical and Computational Fluid Dynamics*, Vol. 33, No. 3-4, 2019, pp. 359–382. https://doi.org/10.1007/s00162-019-00498-8, URL https://doi.org/10.1007/s00162-019-00498-8.

[9] Bitter, N. P., "Stability of Hypervelocity Boundary Layers," Ph.D. thesis, California Institute of Technology, 2015.

[10] Jaisankar, S., and Rao, S. R., "Diffusion regulation for Euler solvers," *Journal of Computational Physics*, Vol. 221, 2007, pp. 577–599. https://doi.org/10.1016/j.jcp.2006.06.030, URL https://doi.org/10.1016/j.jcp.2006.06.030.

[11] Ducros, F., Ferrand, V., Nicoud, F., Weber, C., Darracq, D., Gacherieu, C., and Poinsot, T., "Large-Eddy Simulation of the Shock/Turbulence Interaction," *Journal of Computational Physics*, Vol. 152, No. 2, 1999, pp. 517–549. https://doi.org/10.1006/jcph.1999.6238, URL https://doi.org/10.1006/jcph.1999.6238.

[12] Marineau, E. C., Grossir, G., Wagner, A., Leinemann, M., Radespiel, R., Tanno, H., Wadhams, T. P., Chynoweth, B. C., Schneider, S. P., Wagnild, R., and Casper, K. M., "Compilation and Analysis of Second Mode Amplitudes of Sharp Cones in

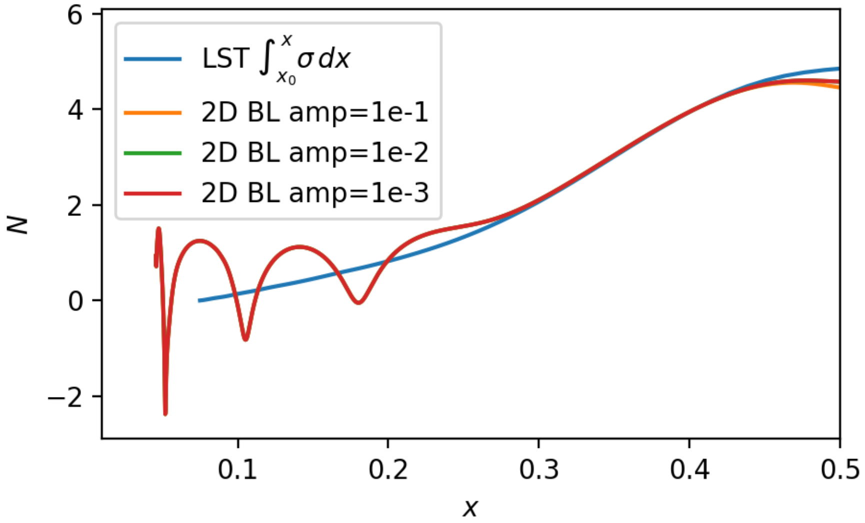

Fig. 6 N factor comparison between LST and SPARC for various amplitudes of perturbations at the inlet boundary. The three SPARC simulations are overlapping lines and may be difficult to differentiate.

Hypersonic Wind Tunnels," *2018 AIAA Aerospace Sciences Meeting*, American Institute of Aeronautics and Astronautics, 2018. https://doi.org/10.2514/6.2018-0349, URL https://doi.org/10.2514/6.2018-0349.

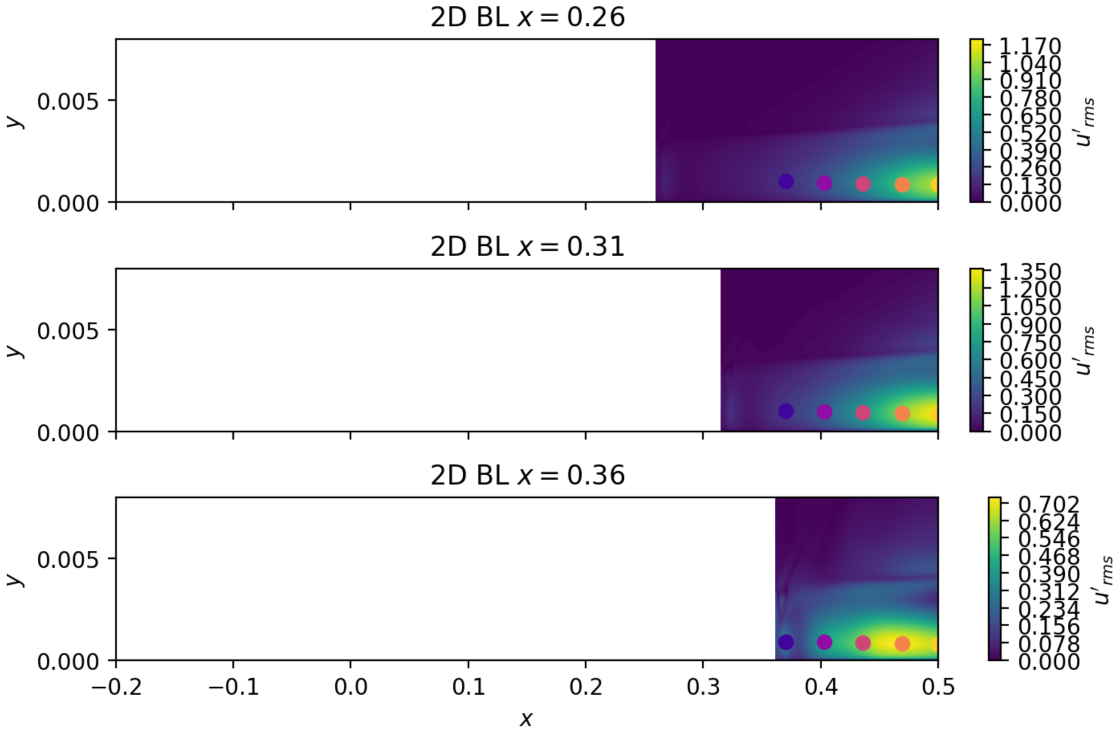

Fig. 7 Streamwise velocity perturbation RMS values for the second case study varying the amplitude on the 2D inlet case. The colored dots indicate the locations of the FT coefficients shown in Fig. 8

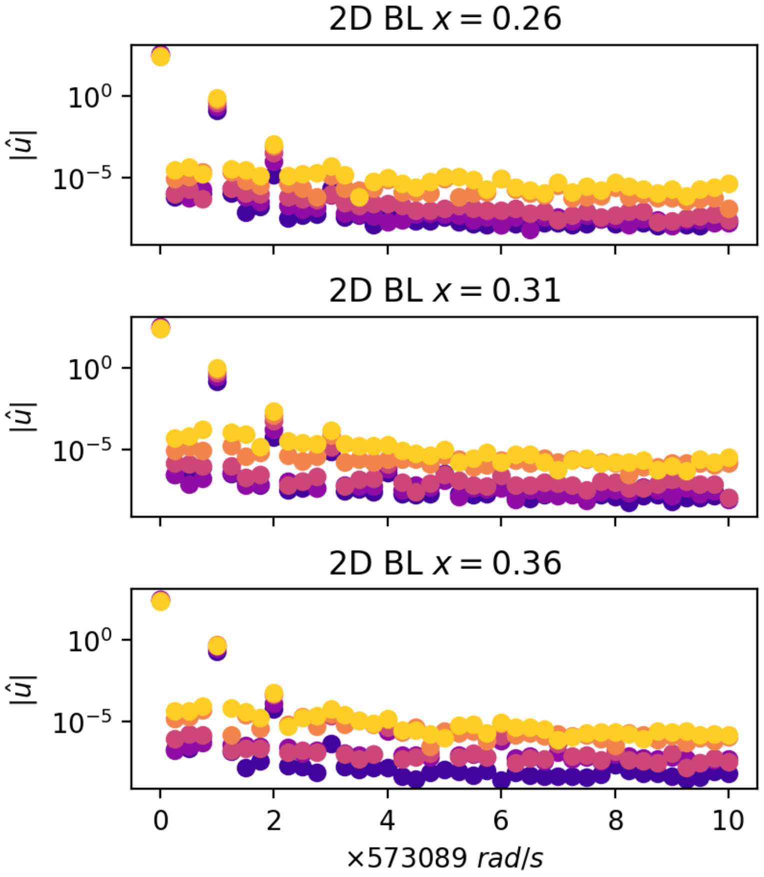

Fig. 8 Streamwise FT coefficient magnitude at the matching colored dots from Fig. 7.

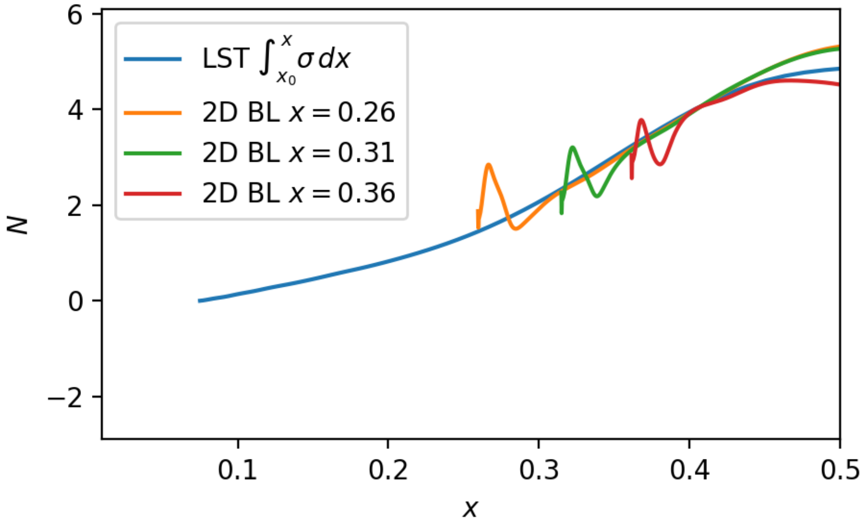

Fig. 9 N factor comparison between LST and SPARC for various streamwise locations of the inlet condition.

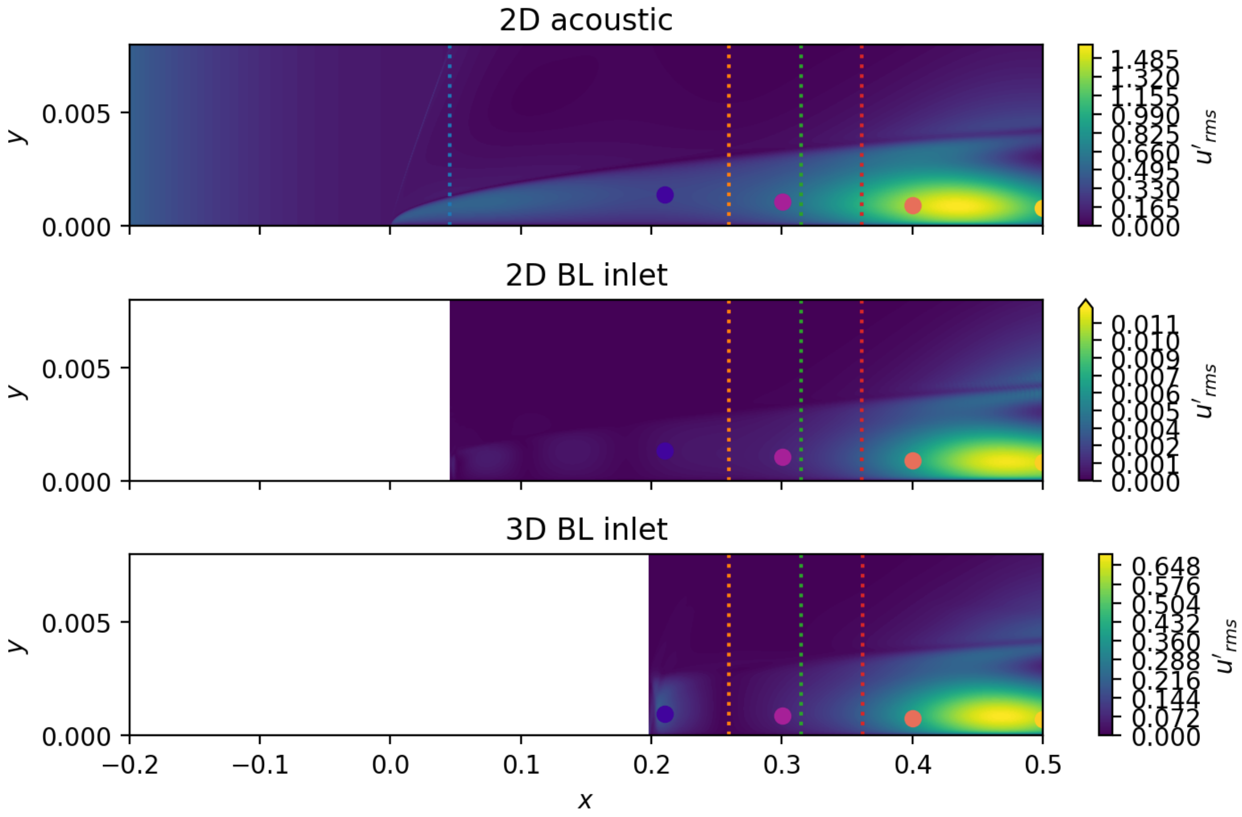

Fig. 10 DNS results using SPARC for the three simulations of the streamwise RMS of the fluctuation. The top acoustic case has the largest upstream domain. The vertical colored lines indicate the locations that match the colored lines of Fig. 12

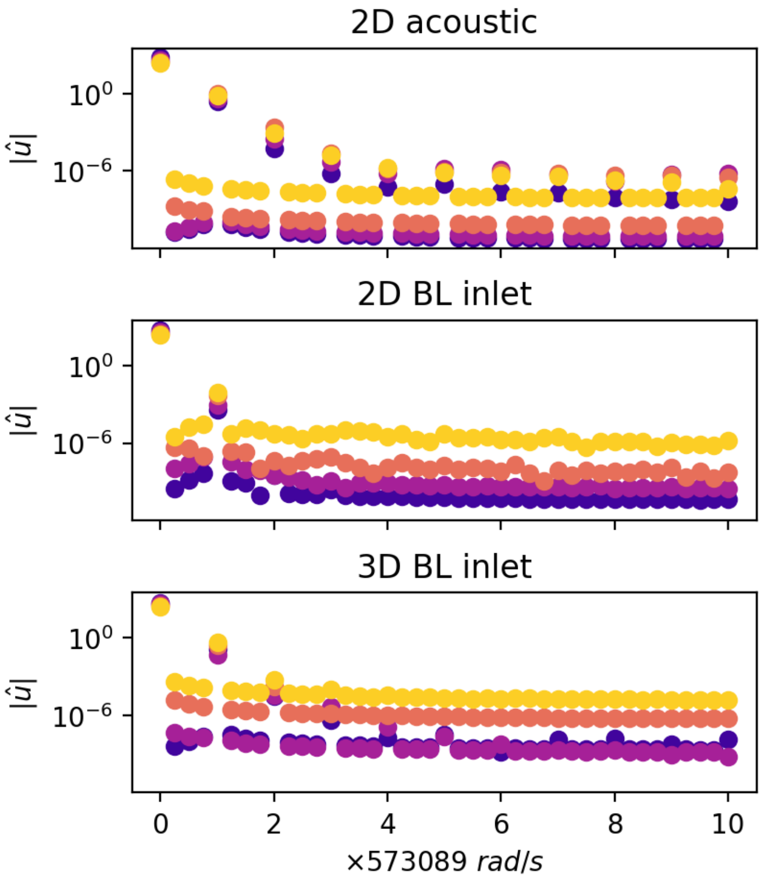

Fig. 11 Streamwise FT coefficient magnitude at the matching colored dots from Fig. 10.

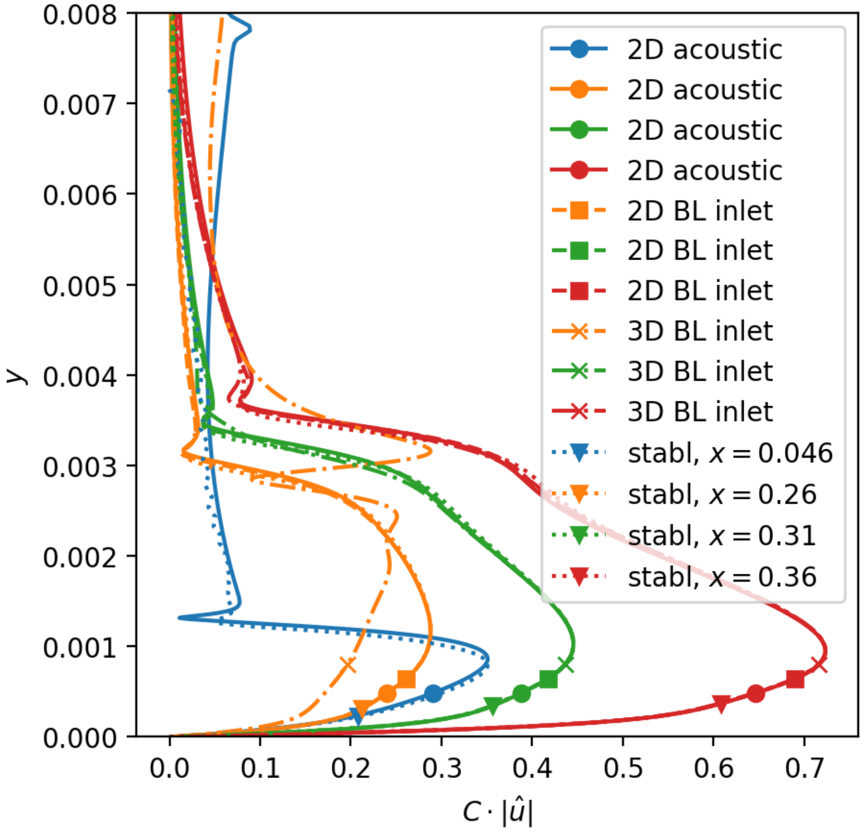

Fig. 12 Fundamental frequency of streamwise velocity Fourier transform from DNS results using SPARC for the final case study. This is compared to the eigenfunction at the same streamwise location as computed using STABL. The color of the lines match the streamwise location of the vertical colored dotted lines shown in Fig. 10

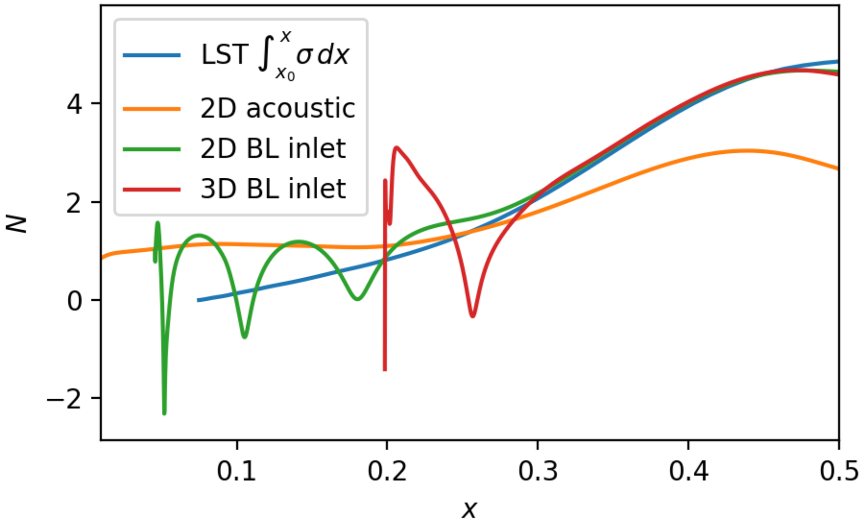

Fig. 13 STABL largest instability mode predicted N-factor compared to the N-factor from the DNS simulations. The frequency is 91.21 kHz and spanwise wavenumber is $\beta = 0/\mathrm{m}$.

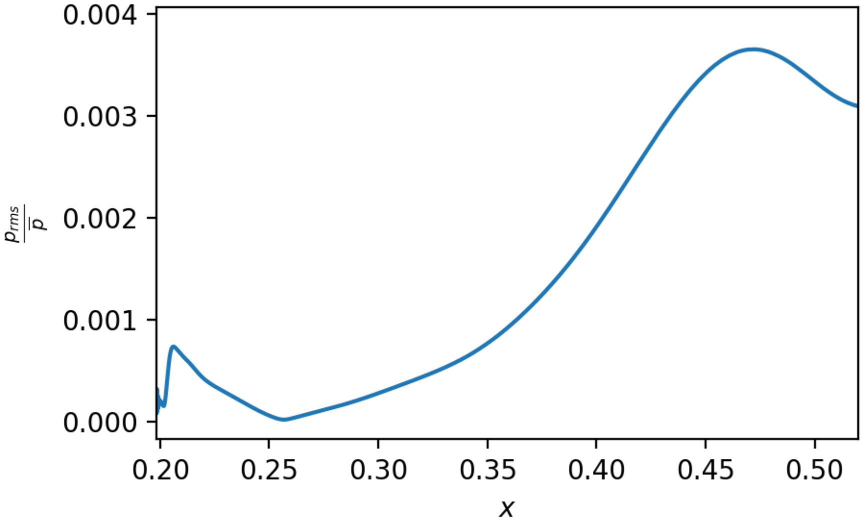

Fig. 14 Wall pressure perturbation RMS of the 3D inlet simulation divided by the average wall presure. This is a good indicator of the amplitude of the eigenfunction relative to the baseflow.